Estimating the magnetization distribution within rectangular rock samples

A. L. A. Reis,[1] V. C. Oliveira Jr.,[1] E. Yokoyama,[2] A. C. Bruno[3] and Pereira,

J. M. B.[3]

---

[1]Department of Geophysics, Observatório

Nacional, Rio de Janeiro, RJ, Brazil.

[2]Institute of Geosciences, University of

Brasília, Brasília, DF, Brazil.

[3]Department of Physics, Pontifical

Catholic University of Rio de Janeiro, Rio

de Janeiro, RJ, Brazil.

Abstract.

Over the last decades, scanning magnetic microscopy techniques have been increasingly used in paleomagnetism and rock magnetism. Different from standard paleomagnetic magnetometers, scanning magnetic microscopes produce high-resolution maps of the vertical component of the magnetic induction field (flux density) on a plane located over the sample. These high-resolution magnetic maps can be used for estimating the magnetization distribution within a rock sample by inversion. Previous studies have estimated the magnetization distribution within rock samples by inverting the magnetic data measured on a single plane above the sample. Here we present a new spatial domain method for inverting the magnetic induction measured on four planes around the sample in order to retrieve its internal magnetization distribution. We have presumed that the internal magnetization distribution of the sample varies along one of its axes. Our method approximates the sample geometry by an interpretation model composed of a one-dimensional array of juxtaposed rectangular prisms with uniform magnetization. The Cartesian components of the magnetization vector within each rectangular prism are the parameters to be estimated by solving a linear inverse problem. Our method automatically deals with the averaging of the measured magnetic data due to the finite size of the magnetic sensor, preventing the application of a deconvolution before the inversion. Tests with synthetic data show the performance of our method in retrieving complex magnetization distributions even in the presence of magnetization heterogeneities. Moreover, they show

26 the advantage of inverting the magnetic data on four planes around the sam-

27 ple adn how this new acquisition scheme improves the estimated magneti-

28 zation distribution within the rock sample. We have also applied our method

29 to invert experimentally measured magnetic data produced by a highly-magnetized

30 synthetic sample that was manufactured in the laboratory. The results show

31 that, even in the presence of apparent position noise, our method was able

32 to retrieve the magnetization distribution consistent with the isothermal re-

33 manent magnetization induced in the sample.

1. Introduction

Based on the estimation of the total (bulk) remanent magnetization (RM), the standard paleomagnetic techniques have been developed for more than 40 years in studies of rock magnetism, magnetostratigraphy and paleogeographic reconstructions [e.g., *Van Der Voo*, 1993]. The evolution of the paleomagnetic techniques is directly linked to the development of rock magnetometers and data processing methods.

Since its beginning in the 1950s, paleomagnetism has seen at least three generation of rock magnetometers [*Turner et al.*, 2015]: astatic systems, spinner magnetometers and superconducting magnetometers. Astatic system was used during the earliest paleomagnetic studies, such as *Blackett* [1952] and *Pozzi and Thellier* [1963], and it was quickly replaced by spinner magnetometers [*Nagata*, 1961]. Spinner magnetometers are most used devices in the paleomagnetic laboratories but they have been systematically replaced by superconducting magnetometers. Superconducting rock magnetometers have been developed since 70s [*Dodson et al.*, 1974; *Goree and Fuller*, 1976], reaching notable sensitivity and quickness of measurements on the last two decade [*Kirschvink et al.*, 2015]. This kind of rock magnetometer can measure both discrete samples (single sample mode) and long-core samples (pass-through mode), with a good spatial accuracy ($\sim$1 cm). The long-core samples or u-channel samples are essential to investigations of magnetostratigraphy and environmental magnetism, such as those ones obtained at IODP (International Ocean Drilling Project).

In terms of data processing, both spinner and SQUID (discrete samples) are similar. For pass-through mode, however, the data processing is little bit different; the measure-

ments are naturally smoothed and have a direct dependence with the sensor response. To overcome this constraint, some studies have used deconvolution algorithms to recover the paleomagnetic signal [*Jackson et al.*, 2010; *Oda and Xuan*, 2014]. Even though the deconvolution methods have been improved on the last years [*Jackson et al.*, 2010; *Lascu et al.*, 2012], *Lascu et al.* [2012] have noticed that there is a resolution constraint related with sensor response. They have compared the measurements of long-core with the discrete (slices samples) synthetic samples and they realize that the sensor setting imposes a spatial resolution limit of 1 cm. Along these lines this method has constraint in studies that need very high spatial or temporal resolution, such as the secular variation recorded in stalagmites or manganese crusts.

In this context, new methods have been developed over the last decades to get around these limitations, in special, the Scanning Magnetic Microscopy (SMM) techniques [*Kirschvink et al.*, 2008; *Oda et al.*, 2011; *Fu et al.*, 2014]. Different from standard paleomagnetic magnetometers, the SMM devices produce high-resolution maps of the vertical component of the magnetic induction field on a planar surface located over the sample. Usually, the scanning magnetic microscopes based on superconducting quantum interference device (SQUID) sensors achieve the best field sensitivity for geoscientific research. However, these devices are very expensive to build/operate and require specific technologies to keep the sensor at cryogenic temperatures and also present a limited sensor-to-sample distance ≈ 100 μm [*Baudenbacher et al.*, 2003; *Fong et al.*, 2005]. Despite of these technical difficulties, SQUID sensors have been successfully applied in several paleomagnetic studies [*Gattacceca et al.*, 2006; *Weiss et al.*, 2007a; *Oda et al.*, 2011; *Fu et al.*, 2014; *Kirschvink et al.*, 2015]. To avoid the problems related with the

SQUID complexity, numerous studies have been attempted to develop alternative low-cost high-performance SMM instruments based on magneto-impedance (MI) [*Uehara and Nakamura*, 2007, 2008], giant magnetoresistance (GMR) [*Hankard et al.*, 2009] and magnetic tunnel junction (MTJ) [*Lima et al.*, 2014] sensors. Compared with SQUID's, these alternative sensors are less sensitive. On the other hand, they are generally easier to operate, operate at room temperature, may achieve higher spatial resolution and also a reduction in the sensor-to-sample distance.

Paleomagnetic techniques usually separate the original rock sample mechanically and estimate the magnetization of resultant small sub-samples. In contrast, SMM allows a non-destructive characterization of the internal magnetization distribution of rock samples by inverting high-resolution magnetic data that is measured around the sample. SMM may provide huge data sets and, consequently, the inverse problems aiming at estimating the magnetization within the samples require efficient matrix algorithms. It is also well known that inverse problems aiming at estimating the magnetization distribution in planar or 3D, e.g., cylindrical and rectangular, rock samples are generally non-unique owing to an infinite number of magnetization distributions produce the same observed field. Moreover, the observed magnetic data are always noise-corrupted and is measured by magnetic sensors having limited sensitivity [*Egli and Heller*, 2000; *Baratchart et al.*, 2013; *Lima et al.*, 2013], contributing to the ill-conditioning of such inverse problems. The inherent ill-conditioning of such inverse problems can be narrowed, for example, by introducing *a priori* information regarding the magnetization distribution and/or by optimizing the geometry of the data acquisition. The introduction of *a priori* information aiming at constraining the possible estimated magnetization distributions and also making them stable to small changes in the

observed data is generally called regularization [*Tikhonov and Arsenin*, 1977; *Engl et al.*, 1996; *Aster et al.*, 2005]. The regularization in the wavenumber domain is generally more tricky than in the space domain. On the other hand, methods in space domain require the solution of large-scale linear systems whereas those ones in wavenumber domain take advantage of the Fast Fourier Transform (FFT) algorithms.

Generally, SMM paleomagnetic studies estimate the approximately 2D magnetization distribution within planar rock samples (usually thin sections) by inverting the magnetic data measured on a parallel plane located over it. The pioneer study of *Egli and Heller* [2000] presents a method, in the wavenumber domain, aiming at retrieving the particular magnetization component that is perpendicular to the planar sample. These authors adapted the method proposed by *Mareschal* [1985] and formulated their problem as a two-dimensional deconvolution, which is solved by applying the FFT. By following a similar approach in the wavenumber domain, *Lima et al.* [2013] presented an efficient method attempted to estimate the magnetization intensity distribution within a planar rock sample having a previously defined constant magnetization direction. The method developed by *Lima et al.* [2013] also uses two-dimensional signal processing methods to regularize the inverse problem, tame noise amplification and improve non-negativity.

A different approach proposed by [*Weiss et al.*, 2007b] in space domain approximates the sample by a discrete set of dipoles. The Cartesian components of the dipoles approximating the sample are estimated by iteratively solving a large linear inverse problem. This method is an adaptation of the well-known equivalent layer technique, which has long been applied to processing potential-field data in space domain [*Dampney*, 1969; *Emilia*, 1973; *Von Frese et al.*, 1981; *Hansen and Miyazaki*, 1984; *Silva*, 1986; *Leão and Silva*, 1989;

Cordell, 1992; Mendonça, 1992; Mendonça and Silva, 1994, 1995; Guspí and Novara, 2009; Li and Oldenburg, 2010; Barnes and Lumley, 2011; Oliveira Jr. et al., 2013; Kara et al., 2014; Li et al., 2014; Barnes, 2014]. The study developed by [Weiss et al., 2007b] represents the first space-domain technique for inverting SMM data. Usui et al. [2012] presented an hybrid method combining useful features of space- and wavenumber-domain techniques. They described the magnetization distribution in a planar rock sample as a weighted average according to the BackusGilbert formulation. In order to overcome the computational cost of the BackusGilbert method, Usui et al. [2012] implemented the subtractive optimally localized averages (SOLA) method, which was originally proposed to solve large-scale inverse problems in helioseismic. The SOLA method approximates some matrix computations by using the FFT, but does not transform the magnetic data to the Fourier domain.

Here, we propose a new spatial domain inversion method to invert the magnetic induction measured on four orthogonal planes around the sample in order to retrieve its internal magnetization distribution. Our method approximates the sample by an interpretation model composed of a one-dimensional array of juxtaposed rectangular prisms with uniform magnetization. The number of rectangular prisms making up the interpretation model is specified by the interpreter and the Cartesian components of the magnetization vector within each rectangular prism are the parameters to be estimated by solving a linear inverse problem.

By imposing this finite one-dimensional magnetization distribution, we constraint the mathematically possible solutions, which results in a regularization by discretization [Engl et al., 1996; Aster et al., 2005]. Moreover, the use of magnetic data measured on more

than one plane around the sample adds independent information about its internal mag-

netization distribution, which also contributes to stabilize the inverse problem. We also

presents a new approach for automatically including the averaging of the magnetic data

over the finite active area of the magnetic sensor. This new approach precludes the ap-

plication of a deconvolution for removing this averaging effect before the inversion. In

comparison with previous methods, the method proposed here does not deal with large-

scale inverse problems because our interpretation model is described by a relatively few

number of parameters.

We have inverted magnetic data produced by numerical simulations with the purpose

of illustrating not only the good performance of our method in ideal cases, but also how

the estimated magnetization distribution obtained by our method can be negatively im-

pacted by the presence of position noise, errors in the sensor-to-sample distance and pre-

processing errors in the observed data. Our results also show the benefit of inverting a full

data set formed by magnetic data measured on four planes around the sample. Tests with

synthetic data simulating a real ferro-manganese crust with magnetization heterogeneities

show that our method can be used, for example, in fine-scale magnetostratigraphic studies.

We have also shown the results obtained by applying our method to invert experimen-

tally measured magnetic data produced by a highly-magnetized synthetic sample that was

manufactured in laboratory. The results show that our method is able to estimate a mag-

netization distribution that is consistent with the Isothermal Remanence Magnetization

(IRM) induced in the sample, even by inverting a magnetic data set that is contaminated

by apparent position noise and were measured by a custom-made magnetometer based on

a Hall sensor.

2. Methodology

2.1. Observed data vector

Let's consider a rectangular rock sample with side lengths equal to L_x, L_y e L_z along, respectively, the x-, y- and z-axes of a Cartesian coordinate system whose origin coincides with the center of the sample (Fig. 1). This coordinate system is conveniently called "main coordinate system" (MCS). We assume that the internal magnetization distribution of the sample varies along the x-axis of the MCS. We also considered four mutually orthogonal planes that are located at the same distance h from the sample surface and are identified by an index $\alpha = 0, 1, 2, 3$ (Figs. 2 and 3). On each plane, there are N measurements of a specific β-component of the magnetic induction, $\beta = y, z$, which is perpendicular to the sample surface and is referred to the MCS.

Let $\mathbf{d}_\beta^\alpha$, $\beta = y, z$, $\alpha = 0, 1, 2, 3$, be $N \times 1$ vectors whose ith element is the β-component of the magnetic induction which is measured at the observation point $(x_i^\alpha, y_i^\alpha, z_i^\alpha)$, $i = 1, ..., N$, on the plane α. For convenience, these vectors are all grouped into the $4N \times 1$ observed data vector $\mathbf{d}$ given below:

$$\mathbf{d} = \begin{bmatrix} \mathbf{d}_z^0 \\ \mathbf{d}_y^1 \\ \mathbf{d}_z^2 \\ \mathbf{d}_y^3 \end{bmatrix} . \tag{1}$$

In practical situations, however, we are not able to measure the magnetic induction produced by the sample at a point. Due to the finite size of the magnetic sensors, what is actually measured is the magnetic induction averaged on the area (or volume) of the magnetic sensor. In the subsection 2.3, we present an analysis of this averaging effect.

2.2. Transformations from the local coordinate systems (LCS's) to the MCS

183   The Cartesian coordinates as well as the magnetic induction components in the observed

184   data vector $\mathbf{d}$ (equation 1) are referred to the MCS (Figure 1). However, the measurements

185   are taken in a different local coordinate system (LCS) for each observation plane (Figures

186   3b-e) and must be subsequently converted to the MCS (Figure 3a). This coordinate

187   transformation is needed because the usual magnetic sensors senses the vertical component

188   of the magnetic induction produced by the sample on a plane located over it. For this

189   reason, the magnetic data on the four observation planes (Figure 2) are obtained by

190   successively rotating the sample through $90°$ intervals around its major axis (x-axis in

191   Figure 1). By repeating this rotating procedure and maintaining the same distance h

192   between the observation plane and the sample surface, its possible to obtain the magnetic

193   induction on the four observation planes (Figures 2). The LCS on each plane has axes x',

194   y' and z' (Figure 3b-e), where the x'-axis coincides with the x-axis of the MCS.

Note that this rotating procedure provides, on each observation plane, the component

of the magnetic induction along the z'-axis of the respective LCS (Figure 3b-e). For

convenience, let us denote the measured z'-component data as a $4N \times 1$ vector given by

$$\mathbf{d}' = \begin{bmatrix} \mathbf{d}_{z'}^{0} \\ \mathbf{d}_{z'}^{1} \\ \mathbf{d}_{z'}^{2} \\ \mathbf{d}_{z'}^{3} \end{bmatrix}, \tag{2}$$

195   where $\mathbf{d}_{z'}^{\alpha}$, $\alpha = 0, 1, 2, 3$, are $N \times 1$ vectors whose ith element is the z'-component of the

196   magnetic induction which is measured at the ith observation point, $i = 1, ..., N$, on the

197   plane α (Figure 3). It is easier, however, converting the measured data $\mathbf{d}'$ (equation 2),

198   referred to the LCS's, to the observed data vector $\mathbf{d}$ (equation 1), which is referred to the

199   MCS.

The geometrical relationships between the LCS's and MCS are shown in Figure 3. Table 1 shows how to perform this coordinate transformation. Let's consider, for example, the measurements obtained on the observation plane $\alpha = 1$ (Figures 2b and 3c). According to this table, the opposite of the measured z'-component data correspond to the y-component of the magnetic induction that would be measured in the MCS; the opposite of the Cartesian coordinates along the z'-axis correspond to the Cartesian coordinates along the y-axis in the MCS; the Cartesian coordinates along the y'-axis correspond to the Cartesian coordinates along the z-axis in the MCS. The other lines of Table 1 contain the relationships used to convert the data obtained on the other planes. Hereafter, it is implicit that all quantities with prime (') are referred to the LCS's while all the quantities without prime (') are referred to the MCS.

2.3. Sensor active area

As pointed out at the end of the subsection 2.1, magnetic sensors do not measure the magnetic induction field at a point. They measure instead the field averaged over the sensor active area (or volume), which is equivalent to a convolution of the magnetic induction field with the sensor answer function [*Roth et al.*, 1989; *Egli and Heller*, 2000; *Lima et al.*, 2013]. The sensor-to-sample distance and the effective area (or volume) are important limiting factors determining the spatial resolution of magnetic sensors.

The magnetic sensors used in paleomagnetic applications have different active area (or volume). *Uehara and Nakamura* [2007, 2008] presented a magneto-impedance (MI) sensor whose cylindrical active volume has 36 μm in diameter and 5500 μm in length, which limits its spatial resolution if compared with the giant magnetoresistance (GMR) sensor presented by *Hankard et al.* [2009] and the magnetic tunnel junction (MTJ) sensor

presented by *Lima et al.* [2014], for example. These two sensors are considered planar and have active areas of, respectively, 9 μm $\times$ 36 μm and $\approx$ 4 μm $\times$ 2 μm. Finally, *Fong et al.* [2005] used a custom-designed low-transition-temperature superconducting quantum interference device (low T$_c$ SQUID) sensor which is also considered planar and has an active area with effective diameter of 80 μm. This is currently one of the most powerful magnetic sensors.

In the following, we present an analysis of the averaging effect produced by the finite size of sensors. For convenience, we limit our study to square-planar sensors which are parallel to the sample surface and have an active area A (Figure 5a). Let us first assume that the sensor detects, at the ith observation point (x_i', y_i', z_i'), $i = 1, ..., N$, located on an observation plane α, $\alpha = 0, ..., 3$, the z'-component of the magnetic induction (flux density) (Figure 3) that is threaded through the active area A (light grey square in Figure 5a) of the sensor. For convenience, let us denote this observed z'-component as $\tilde{d}_i' \equiv \tilde{d}'(x_i', y_i', z_i')$, which represents the ith element of a particular vector $\mathbf{d}_{z'}^{\alpha}$ (equation 2), depending on the observation plane α on which the measurement is done. This observed data $\tilde{d}_i'$ can then be described as a two-dimensional convolution given by

$$\tilde{d}_i' = \int\limits_{-\infty}^{\infty} \int\limits_{-\infty}^{\infty} w(\eta, \zeta) \, d'(x_i' - \eta, y_i' - \zeta, z_i') \, d\eta d\zeta \, , \tag{3}$$

where $w(\eta, \zeta)$ is the sensor answer function [*Egli and Heller*, 2000] and $d'(x_i' - \eta, y_i' - \zeta, z_i')$ represents the theoretical values of the z'-component of the magnetic induction produced by the rock sample at the points located on the observation plane α with constant z_i' (Figure 3). Here, we do not consider the dependence with the sensor-to-sample distance

h (Figure 5a). In this case, the sensor answer function is given by [*Egli and Heller*, 2000]

$$w(x'_i, y'_i) = \begin{cases} 1/A, & (x'_i, y'_i) \in A \\ 0, & (x'_i, y'_i) \notin A \end{cases} . \tag{4}$$

By substituting this sensor answer function into equation 3, we obtain

$$\tilde{d}'_i = \frac{1}{A} \int\limits_{-\infty}^{\infty} \int\limits_{-\infty}^{\infty} d'(x'_i - \eta, y'_i - \zeta, z'_i)\, d\eta d\zeta . \tag{5}$$

Equation 5 has an analytical solution in the wavenumber domain [*Egli and Heller*, 2000].

However, we opted for using an approximated solution in the space domain. This approx-

imation consists in discretizing the integral 5 by using a midpoint rule on a regular grid

of $Q_x \times Q_y$ points $(x'_j, y'_j) \in A$, $j = 1, ..., Q$, where $Q = Q_x Q_y$ (open circles in Figure 5b).

According to this discretization, the active sensor area A is divided into a regular grid of

square cells with area $\Delta A = A/Q$ (Figure 5b). The approximated integral is given by

$$\begin{aligned} \tilde{d}'_i &\approx \frac{1}{A} \sum_{j=1}^{Q} d'_j \, \Delta A \\ &\approx \frac{1}{Q} \sum_{j=1}^{Q} d'_j \end{aligned} , \tag{6}$$

where d'_j is the theoretical value of the z'-component of the magnetic induction produced

by the rock sample at the point (x'_j, y'_j), $j = 1, ..., Q$ (open circles in Figure 5b).

Equation 6 shows that the z'-component $\tilde{d}'_i$ measured at the ith observation point on a

plane α is approximately given by the averaged magnetic induction produced by the rock

sample over the active area A of the sensor. Consequently, the elements of the observed

data vector $\mathbf{d}$ (equation 1) also represent averaged components of the magnetic induction

over the active area A of the magnetic sensor.

2.4. Pre-processing

Our method presumes that the edges of the sample are aligned with the axes of all LCS's (Figure 3b-e) and also that the center of the sample must be placed right below the origin of all LCS's. Notwithstanding, these conditions are not necessarily satisfied in practical situations. Figure 4a illustrates a situation in which these conditions are satisfied. On the other hand, Figure 4b shows a situation in which neither the horizontal coordinates of the center of the sample (black dot) coincide with the origin of the LCS (open dot), nor the edges of the sample are aligned with the axes x' and y' of the LCS. In this case, it is necessary to correct the coordinates $\tilde{x}'$ and $\tilde{y}'$ of the magnetic data on the observation plane with respect to the sample in order to positioning the sample according to the Figure 4a. This correction must be applied to the magnetic data obtained on the four observation planes.

On each observation plane, let's first denote by x'_c and y'_c the horizontal coordinates of the center of the observation plane (represented by the open dot in Figure 4b). Then, the horizontal coordinates $\tilde{x}'$ and $\tilde{y}'$ of each magnetic data on the observation plane are corrected by applying the following transformation:

$$\begin{bmatrix} x' \\ y' \end{bmatrix} = \mathbf{R}^\top \begin{bmatrix} \tilde{x}' - x'_c \\ \tilde{y}' - y'_c \end{bmatrix} + \begin{bmatrix} x'_c \\ y'_c \end{bmatrix} - \begin{bmatrix} \Delta x' \\ \Delta y' \end{bmatrix} \,, \tag{7}$$

where $\Delta x'$ and $\Delta y'$ are the horizontal displacements of the center of the sample with respect to the origin of the respective LCS (Figure 4b),

$$\mathbf{R} = \begin{bmatrix} \cos\theta & \sin\theta \\ -\sin\theta & \cos\theta \end{bmatrix} \,, \tag{8}$$

and θ (Figure 4b) is the angle between the edges of the sample and the horizontal axes x' and y' of the respective LCS. After applying this transformation for correcting the horizontal coordinates $\tilde{x}'$ and $\tilde{y}'$ of each magnetic data on a observation plane, we obtain

₂₄₉ the corrected coordinates x' and y', which are placed on a different area represented by

₂₅₀ the grey rectangle in Figure 4c.

₂₅₁   This transformation must be applied to the magnetic data on the four observation

₂₅₂ planes, before the previously described transformations from the LCS's to the MCS. We

₂₅₃ would like to stress that the transformation described in equations 7 and 8 requires the

₂₅₄ knowledge of the angle θ and also the displacements $\Delta x'$ and $\Delta y'$ (Figure 4b). In practical

₂₅₅ situations, these values are easily estimated by trial-and-error. Finally, on each observa-

₂₅₆ tion plane, the magnetic data are subtracted from its mean value in order to remove the

₂₅₇ effect of a possible (weak) interfering field.

2.5. Interpretation model and forward problem

₂₅₈   We consider that the rock sample can be approximated by an interpretation model con-

₂₅₉ sisting of P uniformly magnetized prisms, which are juxtaposed along the x-axis (Figure

₂₆₀ 1). The kth prism, $k = 1, ..., P$, has the same side lengths L_y and L_z of the sample along,

₂₆₁ respectively, the y- and z-axes (Figure 1). However, its side length along the x-axis is

₂₆₂ specified by the interpreter, so that the total side length of the interpretation model along

₂₆₃ this axis is equal to L_x (Figure 1).

Let's define the $3P \times 1$ parameter vector $\mathbf{m}$ as follows:

$$\mathbf{m} = \begin{bmatrix} \mathbf{m}^1 \\ \vdots \\ \mathbf{m}^P \end{bmatrix}, \tag{9}$$

where

$$\mathbf{m}^k = \begin{bmatrix} m_x^k \\ m_y^k \\ m_z^k \end{bmatrix}, \tag{10}$$

₂₆₄ is a 3×1 vector containing the Cartesian components m_x^k, m_y^k and m_z^k (in A/m) of the

₂₆₅ magnetization vector of the k-prism, $k = 1, \ldots, P$.

266   Let's also define $N \times 1$ coordinate vectors $\mathbf{x}^\alpha$, $\mathbf{y}^\alpha$ and $\mathbf{z}^\alpha$, whose ith elements are the

267   coordinates x_i^α, y_i^α and z_i^α, respectively, of the ith observation point on the plane α (black

268   circle in Figure 5b). Additionally, consider the $QN \times 1$ coordinate vectors $\tilde{\mathbf{x}}^\alpha$, $\tilde{\mathbf{y}}^\alpha$ and

269   $\tilde{\mathbf{z}}^\alpha$. The first Q elements of these vectors are, respectively, the coordinates x_j^α, y_j^α and z_j^α

270   of a regular grid of points (open circles in Figure 5b) centered at the observation point

271   $(x_1^\alpha, y_1^\alpha, z_1^\alpha)$ (black circle in Figure 5b). Similarly, the next set of Q elements of these

272   vectors are the coordinates of a regular grid of Q points centered at the observation point

273   $(x_2^\alpha, y_2^\alpha, z_2^\alpha)$ and so on. The Cartesian coordinates forming the vectors $\mathbf{x}^\alpha$, $\mathbf{y}^\alpha$, $\mathbf{z}^\alpha$, $\tilde{\mathbf{x}}^\alpha$, $\tilde{\mathbf{y}}^\alpha$

274   and $\tilde{\mathbf{z}}^\alpha$ are referred to the MSC (Figure 3).

  Once the coordinate vectors were defined, we define the β-component, $\beta = y, z$, of the

magnetic induction produced by the k-prism (in nT), at the observation points $\mathbf{x}^\alpha$, $\mathbf{y}^\alpha$

and $\mathbf{z}^\alpha$, are grouped into $N \times 1$ vectors given by

$$\mathbf{b}_\beta(\mathbf{x}^\alpha, \mathbf{y}^\alpha, \mathbf{z}^\alpha, \mathbf{m}^k) = \mathbf{A}\mathbf{M}_\beta^k(\tilde{\mathbf{x}}^\alpha, \tilde{\mathbf{y}}^\alpha, \tilde{\mathbf{z}}^\alpha)\mathbf{m}^k \ , \tag{11}$$

where $\mathbf{A}$ is a $N \times QN$ sparse matrix whose element ij, $i = 1, ..., N$, $j = 1, ..., QN$, is given

by

$$[\mathbf{A}]_{ij} = \begin{cases} 1/Q \ , & (i-1)Q < j \leq iQ \\ 0 \ , & \text{otherwise} \end{cases} \tag{12}$$

and

$$\mathbf{M}_\beta^k(\tilde{\mathbf{x}}^\alpha, \tilde{\mathbf{y}}^\alpha, \tilde{\mathbf{z}}^\alpha) = \begin{bmatrix} \partial_{\beta x}\phi_1^k & \partial_{\beta y}\phi_1^k & \partial_{\beta z}\phi_1^k \\ \vdots & \vdots & \vdots \\ \partial_{\beta x}\phi_N^k & \partial_{\beta y}\phi_N^k & \partial_{\beta z}\phi_N^k \end{bmatrix} \tag{13}$$

is a $QN \times 3$ matrix whose elements $\partial_{\beta x}\phi_j^k$, $\partial_{\beta y}\phi_j^k$ and $\partial_{\beta z}\phi_j^k$, $j = 1, ..., QN$, are second

derivatives, evaluated at the points $\tilde{\mathbf{x}}^\alpha$, $\tilde{\mathbf{y}}^\alpha$ and $\tilde{\mathbf{z}}^\alpha$, of the function

$$\phi^k(x, y, z) = C_m \iiint\limits_{\vartheta^k} \frac{d\epsilon \, d\zeta \, d\eta}{\sqrt{(x-\epsilon)^2 + (y-\zeta)^2 + (z-\eta)^2}} \tag{14}$$

with respect to the variables x, y and z. In equation 14, $C_m = 10^9 \mu_0 / 4\pi$,

$\mu_0 = 4\pi 10^{-7}\ H/m$ is the magnetic permeability of the free space and the integral is

evaluated over the volume ϑ^k of the kth prism. In this work, the second derivatives in

the matrices $\mathbf{M}_\beta^k(\tilde{\mathbf{x}}^\alpha, \tilde{\mathbf{y}}^\alpha, \tilde{\mathbf{z}}^\alpha)$ (equation 13) are calculated by using the formulas presented

by *Nagy et al.* [2000]. Notice that the vectors $\mathbf{b}_\beta(\mathbf{x}^\alpha, \mathbf{y}^\alpha, \mathbf{z}^\alpha, \mathbf{m}^k)$ (equation 11) contain

averaged values of the β-components of the magnetic induction produced by the inter-

pretation model at the observation points located at the four planes $\alpha = 0, 1, 2, 3$. The

averaging is imposed by the matrix $\mathbf{A}$ defined in equation 12.

From equation 11, we define the $N \times 1$ vectors $\mathbf{B}_\beta^\alpha(\mathbf{m})$ containing the β-component of

the magnetic induction produced by all prisms forming the interpretation model on each

plane α as follows:

$$\mathbf{B}_\beta^\alpha(\mathbf{m}) \equiv \sum_{k=1}^{P} \mathbf{b}_\beta(\mathbf{x}^\alpha, \mathbf{y}^\alpha, \mathbf{z}^\alpha, \mathbf{m}^k) . \tag{15}$$

By grouping all these vectors $\mathbf{B}_\beta^\alpha(\mathbf{m})$, we define the $4N \times 1$ theoretical-predicted data

vector

$$\mathbf{B}(\mathbf{m}) = \begin{bmatrix} \mathbf{B}_z^0(\mathbf{m}) \\ \mathbf{B}_y^1(\mathbf{m}) \\ \mathbf{B}_z^2(\mathbf{m}) \\ \mathbf{B}_y^3(\mathbf{m}) \end{bmatrix} . \tag{16}$$

Finally, by substituting equation 11 into equation 15 and rearranging the terms within

the summation, we can conveniently rewrite the predicted data vector $\mathbf{B}(\mathbf{m})$ (equation

16) as follows:

$$\mathbf{B}(\mathbf{m}) = \mathbf{M}\mathbf{m} , \tag{17}$$

where $\mathbf{M}$ is a $4N \times 3P$ partitioned matrix given by

$$\mathbf{M} = \begin{bmatrix} \mathbf{A}\mathbf{M}_z^1(\tilde{\mathbf{x}}^0, \tilde{\mathbf{y}}^0, \tilde{\mathbf{z}}^0) & \cdots & \mathbf{A}\mathbf{M}_z^P(\tilde{\mathbf{x}}^0, \tilde{\mathbf{y}}^0, \tilde{\mathbf{z}}^0) \\ \mathbf{A}\mathbf{M}_y^1(\tilde{\mathbf{x}}^1, \tilde{\mathbf{y}}^1, \tilde{\mathbf{z}}^1) & \cdots & \mathbf{A}\mathbf{M}_y^P(\tilde{\mathbf{x}}^1, \tilde{\mathbf{y}}^1, \tilde{\mathbf{z}}^1) \\ \mathbf{A}\mathbf{M}_z^1(\tilde{\mathbf{x}}^2, \tilde{\mathbf{y}}^2, \tilde{\mathbf{z}}^2) & \cdots & \mathbf{A}\mathbf{M}_z^P(\tilde{\mathbf{x}}^2, \tilde{\mathbf{y}}^2, \tilde{\mathbf{z}}^2) \\ \mathbf{A}\mathbf{M}_y^1(\tilde{\mathbf{x}}^3, \tilde{\mathbf{y}}^3, \tilde{\mathbf{z}}^3) & \cdots & \mathbf{A}\mathbf{M}_y^P(\tilde{\mathbf{x}}^3, \tilde{\mathbf{y}}^3, \tilde{\mathbf{z}}^3) \end{bmatrix} , \tag{18}$$

where $\mathbf{A}$ is defined in equation 12 and $\mathbf{M}_\beta^k(\tilde{\mathbf{x}}^\alpha, \tilde{\mathbf{y}}^\alpha, \tilde{\mathbf{z}}^\alpha)$, $\beta = y, z$, $\alpha = 0, 1, 2, 3$, $k = 1, \ldots, P$

in equation 13.

Notice that the forward problem presented in this subsection can be easily modified to

the case in which the magnetic data are measured on less than four observation planes.

Besides, this forward problem describes the averaged magnetic induction produced by the

interpretation model at the observation points. The averaging is calculated over a regular

grid of Q points on the active area A of the magnetic sensor (Figure 5).

2.6. Inverse problem

By presuming that the rectangular rock sample can be approximated by our previously described interpretation model, we define the linear inverse problem of estimating

its internal magnetization distribution as a constrained optimization problem. This optimization problem consists in estimating a specific parameter vector $\mathbf{m} = \mathbf{m}^\dagger$ (equation 9)

that minimizes the goal function

$$\Gamma(\mathbf{m}) = \|\mathbf{d} - \mathbf{B}(\mathbf{m})\|_2^2 + \mu_0 \, f_0 \, \|\mathbf{R}\mathbf{m}\|_2^2 , \tag{19}$$

where $\|\cdot\|_2$ stands for Euclidian (or ℓ_2) norm, $\mathbf{d}$ and $\mathbf{B}(\mathbf{m})$ are, respectively, the observed

and predicted data vectors (equations 1 and 17), f_0 is defined as the ratio

$$f_0 = \frac{tr\left(\mathbf{M}^\top \mathbf{M}\right)}{3P} , \tag{20}$$

where $tr\left(\cdot\right)$ stands for the trace, μ_0 is a positive number called regularization parameter and $\mathbf{R}$ is a $3P - 3 \times 3P$ sparse matrix whose ijth-element is given by

$$[\mathbf{R}]_{ij} = \begin{cases} 1\,, & i = j \\ -1\,, & j = i + 3 \\ 0\,, & \text{otherwise} \end{cases} . \tag{21}$$

In equation 19, f_0 is used with the purpose of constraining the practical range of μ_0, which controls the trade-off between the first and second terms at the right side. The first term represents the data fit and the second term is the well-known first-order Tikhonov regularization function [*Aster et al.*, 2005], which imposes "smoothness" to the estimated parameters. The least-squares estimate of the parameter vector $\mathbf{m} = \mathbf{m}^\dagger$ minimizing the goal function (equation 19) is given by

$$\mathbf{m}^\dagger = \left(\mathbf{M}^\top\mathbf{M} + \mu_0\,f_0\,\mathbf{R}^T\mathbf{R}\right)^{-1}\mathbf{M}^\top\mathbf{d}\,. \tag{22}$$

We consider that the estimated parameter vector $\mathbf{m}^\dagger$ given by equation 22 approximates the real magnetization distribution within the rectangular rock sample.

2.7. Software implementation

The inversion method proposed here is implemented in the Python programming language. Our implementation relies on the open-source library numpy [*Jones et al.*, 2001–present; *Walt et al.*, 2011, `http://scipy.org`] for array-based computations, matplotlib [*Hunter*, 2007, `http://matplotlib.org`] for plots and maps, and Fatiando a Terra [*Ueda et al.*, 2013, `http://www.fatiando.org`] for implementing the forward problem.

The computational experiments (e.g., data processing, synthetic tests, real data application) were performed in Jupyter (formerly IPython) notebooks [*Pérez and Granger*, 2007, `http://jupyter.org/`]. The notebook files combine the source code, the results and figures generated by the code and rich text to explain the analysis.

All source code, Jupyter notebooks, data, and results can be found at the online reposi-
tory `https://github.com/pinga-lab/magnetization-rock-sample` (**Note to review-
ers: the online repository will be made public upon publication**). An archived
version of this repository is also available at `http://dx.doi.org/...` (**Note to review-
ers: the archived version will be uploaded upon publication**).

3. Numerical simulations

3.1. Highly magnetized sample

We have applied our method to invert the synthetic data produced by a simulated rock
sample (not shown) with $L_x = 16$ mm and $L_y = L_z = 3$ mm, according to the Figure
1. This synthetic sample is formed by $P = 16$ juxtaposed prisms along the x-axis, where
each prism has a uniform and high magnetization (red dots in Figures 7, 9 and 11). In
all tests presented in this section, the simulated magnetic sensor has an square active
area $A = (300 \, \mu\text{m})^2$, which was discretized into a regular grid of 7×7 points, totalling
$Q = 49$ (Figure 5). The magnetic data produced by the synthetic sample on each plane
$\alpha = 0, 1, 2, 3$ were calculated at $N = 4,284$ points, on a set of 42 regularly spaced lines
that are parallel to the x-axis, each one with 102 regularly spaced points. The data were
also contaminated with a pseudo-random Gaussian noise having null mean and standard
deviation equal to $30,000 \, \mu\text{T}$. These data simulate an observed data set. Besides, we have
simulated the misalignment problems described in the subsection 2.4. Table 2 shows the
parameters θ, $\Delta x'$ and $\Delta y'$ (Figure 4b) representing these misalignments in the magnetic
data produced by the synthetic sample on the planes $\alpha = 0, 1, 2, 3$.

3.1.1. Validation test

321   In this test, the simulated noise-corrupted data were calculated by keeping the distance

322 h (Figure 3) between all the planes and the surface of the sample equal to 500 μm. The

323 noise-corrupted magnetic data were properly corrected from the misalignment problems

324 by using the parameters shown in Table 2 and the equations 7 and 8. These magnetic

325 data (Figures 6a, d, g and j) were inverted by our method in order to retrieve the internal

326 magnetization distribution of the synthetic sample (red dots in Figures 7, 9 and 11). To

327 do that, we used an interpretation model which has side lengths L_x, L_y and L_z equal to

328 the true ones and is formed by the same number of prisms ($P = 16$) as the synthetic

329 sample.

330   Figure 7 shows the four estimated magnetization distributions obtained by our method.

331 The one obtained by inverting the magnetic data on the four planes $\alpha = 0, 1, 2, 3$ is

332 represented by the black dots and dashed lines. The three sets of blue dots and dashed

333 lines represent the estimated magnetization distribution obtained by inverting the data

334 located on the plane $\alpha = 0$, planes $\alpha = 0, 1$ and planes $\alpha = 0, 1, 2$, which are plotted,

335 respectively, with high, intermediate and low transparency. All these estimates were

336 obtained by using a regularization parameter $\mu_0 = 1 \times 10^{-10}$ (equation 19). We can

337 see that the estimated magnetization distribution obtained by inverting the full data

338 set (black dots and black dashed lines in Figure 7) is the best one in retrieving the

339 true magnetization distribution (red dots and red lines in Figure 7). This estimated

340 magnetization distribution yields a predicted data (Figures 6b, e, h and k) that is very

341 close to the observed data (Figures 6a, d, g and j). The normalized histograms of the

342 residuals between the predicted and observed data (Figures 6c, f, i and l) show sample

343 means μ and sample standard deviations σ very close to that ones of the pseudo-random

344 noise contaminating the simulated magnetic data.

345 These results show the advantage of inverting the full data set (data on the four planes)

346 and also the good performance obtained by our method if all the premisses about the

347 magnetic data and the sample are not violated.

348 **3.1.2. Pre-processing errors**

349 As in the previous test, the simulated noise-corrupted data used here were calculated

350 by keeping the distance h (Figure 3) between all the planes and the surface of the sample

351 equal to 500 μm. On the other hand, we have not corrected the misalignment problems

352 by using the parameters shown in Table 2 and the equations 7 and 8. We have also

353 introduced a different constant bias into the misaligned magnetic data on each plane

354 with the purpose of simulate errors in the pre-processing stage. These bias are equal to

355 $-26,000$ μT, $-10,000$ μT, $-26,000$ μT and $-23,000$ μT for the magnetic data on the

356 planes $\alpha = 0, 1, 2$ and 3, respectively. As in the previous test, we applied our method by

357 using an interpretation model with side lengths L_x, L_y and L_z equal to the true ones and

358 with the same number of prisms ($P = 16$) as the synthetic sample along the x-axis.

359 Figure 9 confirms the the superiority of the estimated magnetization distribution ob-

360 tained by inverting the full data set (black dots and black dashed lines) over the remaining

361 three (blue dots and blue dashed lines). All these estimates were obtained by using a reg-

362 ularization parameter $\mu_0 = 5 \times 10^{-2}$ (equation 19). We can see, however, that even the

363 estimate obtained with the full data set failed in retrieving the magnetization distribution

364 of the simulated sample (red dots). This poorly-estimated magnetization distribution

365 yields predicted data (Figures 8b, e, h and k) that do not recover the observed data (Fig-

ures 8a, d, g and j). This coarse data fit is shown by the normalized histograms of the

residuals between the predicted and observed data (Figures 8c, f, i and l). The sample

means μ would be very close to the simulated constant bias and the sample standard

deviations σ would be very close to that one of the pseudo-random noise if the magnetic

data were properly corrected from the misalignment problems.

These results exemplify the effects of not correcting the misalignment problems prior

to the inversion. Besides, they show the advantage of inverting the full data set (data

on the four planes). As we can see, these problems lead to an estimated magnetization

distribution that do not retrieves the true one and also produce a coarse data fit.

3.1.3. Sensor-to-sample distance

Unlike the previous tests, the distance h (Figure 3) between the surface of the sample

and the observation points at each plane is not constant. On each plane $\alpha = 0, 1, 2, 3$,

the observation points are located on a set of 42 regularly-spaced acquisition lines, each

one with 102 regularly spaced points. In this test, the distance h is contaminated with a

Gaussian position noise having a common standard deviation of 100 μm and a different

mean value equal to 420 μm, 330 μm, 400 μm and 230 μm on each plane $\alpha = 0, 1, 2, 3$,

respectively. The distance h, however, is constant for observation points located on the

same acquisition line.

The noise-corrupted magnetic data were properly corrected from the misalignment prob-

lems by using the parameters shown in Table 2 and the equations 7 and 8. As in the

previous tests, we applied our method by using an interpretation model with side lengths

L_x, L_y and L_z equal to the true ones and with the same number of prisms ($P = 16$) as

the synthetic sample along the x-axis. We have applied our method to invert the noise-

corrupted magnetic data without, however, consider the variations in the sensor-to-sample

distances h. Instead, we presumed a constant distance $h = 500$ μm between all the planes

and the surface of the sample.

Figure 11 shows the four estimated magnetization distributions produced in this test.

All these estimates were obtained by using a regularization parameter $\mu_0 = 1 \times 10^{-10}$

(equation 19). This figure also shows that, as in the previous tests, the estimate obtained

by inverting the full data set (black dots and black dashed lines) best approximates the

true magnetization distribution (red dots and red lines). However, even this estimate

did not completely retrieved the magnetization distribution of the synthetic sample (red

dots). Notice that the observed data (Figures 10a, d, g and j) present striations aligned

with the acquisition lines on each observation plane. These striations are produced by the

presence of position noise in the observation points. Despite these striations, the (almost

good) estimated magnetization distribution obtained by inverting the full data set (black

dots and black dashed lines in Figure 11) yields predicted data (Figures 10b, e, h and k)

that recover the observed data (Figures 10a, d, g and j) in an acceptable manner. This

acceptable data fit is shown by the normalized histograms of the residuals between the

predicted and observed data (Figures 10c, f, i and l). The sample means μ are close to

zero but the sample standard deviations σ present some discrepancies with respect to

that one of the pseudo-random noise in magnetic data. According to these histograms,

the poorest data fit occurs in the observation plane $\alpha = 3$ (Figure 10l), where the sample

standard deviation $\sigma \approx 60$ μT.

These results illustrate the effects of errors in the sensor-to-sample distance and also

illustrate the advantage of inverting the full data set (data on the four planes). If compared

with the results obtained in the previous test, the results obtained here suggest that our method is most robust against errors in the sensor-to-sample distance than against misalignment errors.

3.2. Marine ferro-manganese crust sample

The method proposed by *Oda et al.* [2011] uses SQUID microscopy to identify the boundaries of fine magnetic stripes (smaller than 1 mm) with approximately reversed magnetization. These magnetic stripes are then correlated with a standard magneto-stratigraphic time scale, providing a tool for estimating ages and growth rates for hydro-genetic ferro-manganese crusts with unprecedented spatial resolution. *Oda et al.* [2011] applied their method to analyse a block of ferro-manganese crust obtained from a seamount in the Northwest Pacific Ocean. They have cut and sliced a columnar block parallel to the growth lamination at 1.5 mm intervals using a 0.3-mm-thick diamond-wire saw. After that, the magnetization of the slices have been estimated by using a SQUID magnetome-ter. Note that, to determine the magnetization along the sample, it was necessary to slice it in small parts. It would be useful instead to determine the bulk magnetization along the sample by using a non-destructive method. Here, we present a feasibility study aiming at determining the magnetization distribution along a simulated sample by apply-ing our method and directly inverting the high-resolution measurements of the magnetic induction around the sample.

The internal magnetization distribution of our simulated sample is based on the real magnetization distribution within the ferro-manganese crust presented by *Oda et al.* [2011]. Our sample (not shown) is formed by $P = 24$ juxtaposed prisms along the x-axis and has side lengths equal to $L_x = 36$ mm, $L_y = 5$ mm and $L_z = 5$ mm along,

₄₃₄ respectively, the x, y and z axes. Figure 13 shows the magnetization of these prisms

₄₃₅ (red dots) along the x-axis of the sample. We have also simulated the presence of 20

₄₃₆ magnetized grains that are randomly placed within the sample. These grains are rep-

₄₃₇ resented by spheres having radius equal to 30 μm, constant magnetization intensity of

₄₃₈ 100 A/m and random magnetization direction. Notice that the presence of these magne-

₄₃₉ tized grains violates the premise that the rock sample can be approximated by uniformly

₄₄₀ magnetized prisms. The magnetic data produced by our heterogeneous sample on each

₄₄₁ plane $\alpha = 0, 1, 2, 3$ were calculated at a constant distance $h = 370$ μm, on a regular grid

₄₄₂ of 200×100 points along the x and y/z axes, respectively, and were also contaminated

₄₄₃ with a pseudo-random Gaussian noise having null mean and standard deviation equal to

₄₄₄ 1.0 nT (Figures 12a, d, g and j). The simulated magnetic sensor used for calculating these

₄₄₅ data has an square active area $A = (300 \, \mu\text{m})^2$, which was discretized into a regular grid

₄₄₆ of 7×7 points, totalling $Q = 49$ (Figure 5).

₄₄₇   Figure 13 shows the four estimated magnetization distributions produced in this test.

₄₄₈ All these estimates were obtained by using a regularization parameter $\mu_0 = 1 \times 10^{-10}$

₄₄₉ (equation 19). This figure also confirms that the estimate obtained by inverting the full

₄₅₀ data set (black dots and black dashed lines) is better than the remaining three (blue dots

₄₅₁ and blue dashed lines) because it completely retrieved the magnetization distribution of

₄₅₂ the simulated heterogeneous sample (red dots). This estimated magnetization distribution

₄₅₃ yields a predicted data (Figures 12b, e, h and k) that is very close to the observed data

₄₅₄ (Figures 12a, d, g and j), except at the regions where the simulated spherical grains are

₄₅₅ close to the sample surface. The normalized histograms of the residuals between the

₄₅₆ predicted and observed data (Figures 12c, f, i and l) show sample means μ and sample

standard deviations σ very close to that ones of the pseudo-random noise contaminating the simulated magnetic data.

As in all the previous tests, these results confirm the advantage of inverting the full data set (data on the four planes). Moreover, they show the good performance of our method in retrieving the magnetization distribution within a complex and heterogeneous synthetic sample simulating a real ferro-manganese crust.

4. Tentative application to real data produced by a synthetic sample

4.1. Sample preparation

We have applied our method to invert experimentally measured data produced by a highly magnetized sample (not shown) that was manufactured in the laboratory of Paleomagnetism of the Institute of Geophysics, Astronomy and Atmospheric Sciences of the University of São Paulo (IAG-USP), in Brazil. The sample is formed by four juxtaposed prisms with side lengths equal to ≈ 4 mm, ≈ 3 mm and ≈ 3 mm along, respectively, the x-, y- and z-axis (with respect to the MCS shown in Figure 1). These prisms were manufactured by filling a rectangular acrylic mould with a magnetite solution and letting it hardens. The magnetite solution is formed by a mixture of a diamagnetic epoxy resin (0.3 g) and colloidal magnetite (0.02 g) obtained from the reaction of ferric sulphate and ferrous chloride. The magnetite has saturation magnetization Ms ranging from 5 Am^2/kg and 8 Am^2/kg. The hardened prisms were then magnetized isothermally by an inducing field of ≈ 1T, according to the schematic representation shown in Figures 14a and b. Finally, the prisms were juxtaposed (Figure 14c), resulting in a sample with side lengths equal to $L_x \approx 16$ mm, $L_y \approx 3$ mm and $L_z \approx 3$ mm. The inclination and declination values of the IRM magnetization within each prism are shown in Table 3.

4.2. Data acquisition

478 The magnetic induction data on the four observation planes around our synthetic sample

479 were measured by a scanning Hall magnetic microscope, developed at Pontifical Catholic

480 University of Rio de Janeiro (PUC-Rio), in Brazil. It is based on a commercial GaAs

481 Hall-effect sensor (HG-176A, AKM Inc.) that detects the remanent magnetic field normal

482 to the scanning plane. The sensor has an active area size of $300\,\mu m$, which is $250\,\mu m$

483 distant from the top of the encapsulation. The maximum spatial resolution achieved

484 is about the size of the sensors active area. The magnetic field sensitivity measured is

485 $350\,nT/Hz^{1/2}$ in the white noise region. The sensor is current biased and pre-amplified by

486 a custom-made electronics at $1.0\,kHz$, and the output Hall voltage is detected by a lock-in

487 amplifier. In our microscope, two independent linear micropositioners (T-LLS260, Zaber

488 Technologies) were oriented perpendicularly and stacked, making up an $x - y$ stage with

489 a maximum travel range of $50\,mm$ in each direction. An acrylic pedestal, $15\,mm$ long,

490 is fixed to the stage, serving two purposes, providing a flat surface for the sample to be

491 mounted to and increasing the distance from the sample to the micropositioners motors

492 minimizing inductive effects. The sensor is mounted on another acrylic rod that can be

493 raised or lowered using a linear actuator (T-LA60A, Zaber Technologies), allowing for the

494 adjustment of the sensor to sample distance with micrometer accuracy. The scanning of

495 the sample is made in a stop-and-go system, meaning that when the sample is moved

496 to a scanning position, it stops for the magnetic field measurement and only then, it

497 goes to the next position. In order to reduce environmental magnetic noise present at

498 the laboratory, the experimental measurements were made inside a small 3 layer open-

499 end magnetic shielded chamber (TLM S-0100, Bartington Instruments). We used for

scanning a step of $200\,\mu m$ in both x and y directions. On each plane $\alpha = 0, 1, 2, 3$, the

magnetic data were measured at a constant distance $h \approx 500\ \mu$m, on a regular grid of

102×42 points along the x and y/z axes, respectively (Figures 15a, d, g and j).

The observed magnetic data were corrected from the apparent misalignment problems

by testing different combinations of parameters θ, $\Delta x'$ and $\Delta y'$ (Figure 4b and equations

7 and 8). The best parameters are very close to those ones shown in Table 2. After that,

the magnetic data sets obtained on each plane were subtracted from their respective mean

values.

4.3. Results and comments

We inverted the observed magnetic data by using an interpretation model which is

formed by $P = 16$ prisms and has side lengths equal to $L_x = 16$ mm, $L_y = 3$ mm and

$L_z = 3$ mm along, respectively, the x, y and z axes. Note that each prism forming the

synthetic sample is approximated by four juxtaposed prisms of the interpretation model.

We considered a square magnetic sensor with active area $A = (300\,\mu\mathrm{m})^2$, which was

discretized into a regular grid of 7×7 points, totalling $Q = 49$ (Figure 5). Figure 16

shows the four estimated magnetization distribution obtained with our method. All these

estimates were obtained by using a regularization parameter $\mu_0 = 1 \times 10^{-10}$ (equation 19).

The black dots and black dashed lines represent the estimate obtained by inverting the

magnetic data on the four observation planes. This estimated magnetization distribution

yields a predicted data (Figures 15b, e, h and k) that recover the main features in the

observed data (Figures 15a, d, g and j). This coarse data fit is shown by the normalized

histograms of the residuals between the predicted and observed data (Figures 15c, f, i

and l). These histograms show non-null sample means μ and different sample standard deviations σ.

Based on the results obtained with synthetic data, this poor data fit may be related to the misalignment problems. Probably, the parameters θ, $\Delta x'$ and $\Delta y'$ (Figure 4b and equations 7 and 8), which were estimated by trial-and-error, do not lead to a suitable correction of the misalignment problems. These problems, however, were possibly worsened by the apparent imprecision in the sensor positioning (or position noise) during the scanning stage. Notice that, as in the numerical test showing the effects of position noise, the observed data (Figures 15c, f, i and l) present striations along the acquisition lines on each observation plane. According to *Lee et al.* [2004], the presence of position noise has an important implication for the design of scanning magnetic microscopy. We have also verified with synthetic data that errors in the sensor-to-sample distance could negatively impact the results obtained by our method.

These results cannot nonetheless be completely rejected owing to the estimated magnetization distribution along the synthetic sample shows two important characteristics.

The first one concerns the estimated magnetization intensities (Figure 16a). As we can see, the estimated intensities exhibit an interesting pattern formed by a well-defined cycle of a low value that is followed by three higher values. This cycle repeats four times, coinciding with the number of prisms forming our synthetic sample. For convenience, grouped the estimated values representing the magnetization within each prism. The low values observed in the estimated magnetization intensities (Figure 16a), as well as the corresponding inclination and declination values (Figures 16b and c), are represented by black triangles. This remarkable pattern is consistent with the magnetite precipitation

during the manufacturing of our sample. This precipitation would decrease the magnetite

concentration at the top of each sample prism, increasing the concentration towards their

bottom. The magnetic induction produced by these low-concentration zones there must

be superimposed by those ones produced by the high-concentration zones, which makes

the correct estimation of the magnetization direction in these low-concentration zones

very difficult. Due to this possible precipitation effect, we did not take into consideration

the estimated values that coincides with the low-concentration zones (black triangles in

Figure 16). Consequently, we based our interpretation on the estimated values that are

not located at the low-concentration zones.

The second interesting characteristic of the estimated magnetization distribution along

the synthetic sample is about the estimated inclination/declination (Figures 16b and c).

Note that the estimated inclinations (blue dots in Figure 16b) within the four prisms

forming the sample are close to the approximated values shown in Table 3. On the other

hand, the estimated declinations (blue dots in Figure 16c) are close to the values shown in

Table 3 at the prisms 0, 1 and 2, but are very different at the prism 3. This discrepancy

nonetheless is not a problem because, at prism 3, the estimated inclination is close to $90°$

(Figure 16b) and, in this case, the estimated declinations are not important.

These results show that, even inverting a magnetic data set that were measured by a

prototype magnetometer and were, at least apparently, highly contaminated with position

noise, our method estimated a magnetization distribution that is consistent with the IRM

orientation within our manufactured sample.

5. Conclusion

We have presented a new method for inverting scanning magnetic microscopy data with the purpose of estimating the internal magnetization distribution of a rectangular rock sample whose internal magnetization distribution varies along one of its axes. Our method presents a new approach for automatically including the averaging effect produced by the finite size of the magnetic sensor. Additionally, our method takes advantage of the geometry of a rectangular sample to propose a new scanning design aiming at providing the magnetic data not only on a single plane over the sample, but on four mutually orthogonal planes located around the sample. The use of magnetic data located on the four planes instead of a single one introduces independent information into the linear system to be solved and consequently leads to a a better conditioned inverse problem. The advantage of inverting magnetic data located on four planes around the sample is confirmed by all tests with synthetic data.

Results with synthetic data produced by a simulated highly-magnetized sample show not only the good performance of our method in retrieving the magnetization distribution within a rock sample in an ideal case, but also how the results obtained by our method are negatively impacted by imprecisions in the sensor positioning (or position noise). Results with synthetic data produced by a simulated sample that resembles a marine ferro-manganese crust having a complex and heterogeneous internal magnetization distribution suggest that our method could be applied to invert magnetic data produced by real geological samples. We have also applied our method to invert experimental magnetic data for estimating the internal magnetization distribution of a synthetic sample that was manufactured in laboratory. Despite the misalignment problems occurred during the

scanning stage and also the apparent high position noise in the experimental magnetic data, our method estimated a meaningful magnetization distribution that is consistent with that one in the manufactured sample.

These results show that our method could be an interesting complement of traditional paleomagnetic techniques aiming at providing a non-destructive diagnostic of geological samples. Nevertheless, further tests using either manufactured and geological samples need to be carried out with the purpose of validating our approach, better evaluating the effects of position noise and misalignment problems during the scanning stage and also developing automatic pre-processing techniques.

By presuming that the internal magnetization of the rectangular sample varies along one of its axis we implicitly restrict the application of our method to samples that are perpendicular to the growth lamination within rocks. It would be interesting to generalize our method in order to remove this restriction and allow its application to estimate complex magnetization distributions within rock samples.

References

610 Aster, R. C., B. Borchers, and C. H. Thurber (2005), *Parameter Estimation and Inverse*

611 *Problems, Volume 90 (International Geophysics)*, Academic Press.

612 Baratchart, L., D. P. Hardin, E. A. Lima, E. B. Saff, and B. P. Weiss (2013), Characteriz-

613 ing kernels of operators related to thin-plate magnetizations via generalizations of hodge

614 decompositions, *Inverse Problems*, *29*(1), 015,004, doi:10.1088/0266-5611/29/1/015004.

615 Barnes, G. (2014), Reconstructing the gravity gradient anomaly field from surveys with

616 wide line spacing using equivalent source processing: an error analysis, *Geophysical*

617 *Prospecting*, *62*(3), 646–657, doi:10.1111/1365-2478.12098.

618 Barnes, G., and J. Lumley (2011), Processing gravity gradient data, *GEOPHYSICS*,

619 *76*(2), I33–I47, doi:10.1190/1.3548548.

620 Baudenbacher, F., L. E. Fong, J. R. Holzer, and M. Radparvar (2003), Monolithic

621 low-transition-temperature superconducting magnetometers for high resolution imag-

622 ing magnetic fields of room temperature samples, *Appl. Phys. Lett.*, *82*(20), 3487–3489,

623 doi:http://dx.doi.org/10.1063/1.1572968.

624 Blackett, P. M. S. (1952), A negative experiment relating to magnetism and the earth's

625 rotation, *Philosophical Transactions of the Royal Society of London A: Mathematical,*

626 *Physical and Engineering Sciences*, *245*(897), 309–370, doi:10.1098/rsta.1952.0024.

627 Cordell, L. (1992), A scattered equivalent-source method for interpolation and gridding of

628 potentialfield data in three dimensions, *GEOPHYSICS*, *57*(4), 629–636, doi:10.1190/1.

629 1443275.

630 Dampney, C. N. G. (1969), The equivalent source technique, *GEOPHYSICS*, *34*(1), 39–

631 53, doi:10.1190/1.1439996.

Dodson, R., M. Fuller, and W. Pilant (1974), On the measurement of the remanent magnetism of long cores, *Geophysical Research Letters*, *1*(4), 185–188, doi:10.1029/ GL001i004p00185.

Egli, R., and F. Heller (2000), High-resolution imaging using a high-tc superconduct-ing quantum interference device (squid) magnetometer, *J. Geophys. Res.: Solid Earth*, *105*(B11), 25,709–25,727, doi:10.1029/2000JB900192.

Emilia, D. A. (1973), Equivalent sources used as an analytic base for processing total magnetic field profiles, *GEOPHYSICS*, *38*(2), 339–348, doi:10.1190/1.1440344.

Engl, H. W., M. Hanke, and A. Neubauer (1996), *Regularization of Inverse Problems (Mathematics and Its Applications)*, Springer.

Fong, L. E., J. R. Holzer, K. K. McBride, E. A. Lima, F. Baudenbacher, and M. Radparvar (2005), High-resolution room-temperature sample scanning superconducting quantum interference device microscope configurable for geological and biomagnetic applications, *Rev. Sci. Instrum.*, *76*(5), doi:10.1063/1.1884025.

Fu, R., E. Lima, and B. Weiss (2014), No nebular magnetization in the allende {CV} carbonaceous chondrite, *Earth Planet. Sci. Lett.*, *404*, 54–66, doi:10.1016/j.epsl.2014. 07.014.

Gattacceca, J., M. Boustie, B. P. Weiss, P. Rochette, E. A. Lima, L. E. Fong, and F. J. Baudenbacher (2006), Investigating impact demagnetization through laser impacts and squid microscopy, *Geology*, *34*(5), 333–336, doi:10.1130/G21898.1.

Goree, W. S., and M. Fuller (1976), Magnetometers using rf-driven squids and their applications in rock magnetism and paleomagnetism, *Reviews of Geophysics*, *14*(4), 591–608, doi:10.1029/RG014i004p00591.

Guspí, F., and I. Novara (2009), Reduction to the pole and transformations of scattered magnetic data using newtonian equivalent sources, *GEOPHYSICS*, *74*(5), L67–L73, doi:10.1190/1.3170690.

Hankard, F., J. Gattacceca, C. Fermon, M. Pannetier-Lecoeur, B. Langlais, Y. Quesnel, P. Rochette, and S. A. McEnroe (2009), Magnetic field microscopy of rock samples using a giant magnetoresistancebased scanning magnetometer, *Geochem., Geophys., Geosyst.*, *10*(10), doi:10.1029/2009GC002750.

Hansen, R. O., and Y. Miyazaki (1984), Continuation of potential fields between arbitrary surfaces, *GEOPHYSICS*, *49*(6), 787–795, doi:10.1190/1.1441707.

Hunter, J. D. (2007), Matplotlib: A 2d graphics environment, *Computing in Science & Engineering*, *9*(3), 90–95, doi:10.1109/MCSE.2007.55.

Jackson, M., J. A. Bowles, I. Lascu, and P. Solheid (2010), Deconvolution of u channel magnetometer data: Experimental study of accuracy, resolution, and stability of different inversion methods, *Geochemistry, Geophysics, Geosystems*, *11*(7), doi:10.1029/2009GC002991.

Jones, E., T. Oliphant, P. Peterson, et al. (2001–present), SciPy: Open source scientific tools for Python, [Online; accessed 2016-06-24].

Kara, I., O. T. Bal, H. Tur, and A. Ates (2014), A new efficient method for topographic distortion correction, analytical continuation, vertical derivatives and using equivalent source technique: Application to field data, *Journal of Applied Geophysics*, *106*, 67–76, doi:10.1016/j.jappgeo.2014.04.011.

Kirschvink, J. L., R. E. Kopp, T. D. Raub, C. T. Baumgartner, and J. W. Holt (2008), Rapid, precise, and high-sensitivity acquisition of paleomagnetic and rock-

magnetic data: Development of a low-noise automatic sample changing system for superconducting rock magnetometers, *Geochemistry, Geophysics, Geosystems*, *9*(5), doi:10.1029/2007GC001856.

Kirschvink, J. L., Y. Isozaki, H. Shibuya, Y. ichiro Otofuji, T. D. Raub, I. A. Hilburn, T. Kasuya, M. Yokoyama, and M. Bonifacie (2015), Challenging the sensitivity limits of paleomagnetism: Magnetostratigraphy of weakly magnetized guadalupianlopingian (permian) limestone from kyushu, japan, *Palaeogeography, Palaeoclimatology, Palaeoecology*, *418*, 75 – 89, doi:10.1016/j.palaeo.2014.10.037.

Lascu, I., M. Jackson, and P. Sølheid (2012), Beyond u-channels: improving the deconvolution of u-channel magnetometer data for non-standard sample geometries, *IRM Quarterly*, *22*(3).

Leão, J. W. D., and J. B. C. Silva (1989), Discrete linear transformations of potential field data, *GEOPHYSICS*, *54*(4), 497–507, doi:10.1190/1.1442676.

Lee, S.-Y., J. Matthews, and F. C. Wellstood (2004), Position noise in scanning superconducting quantum interference device microscopy, *Appl. Phys. Lett.*, *84*(24), 5001–5003, doi:10.1063/1.1763215.

Li, Y., and D. W. Oldenburg (2010), Rapid construction of equivalent sources using wavelets, *GEOPHYSICS*, *75*(3), L51–L59, doi:10.1190/1.3378764.

Li, Y., M. Nabighian, and D. W. Oldenburg (2014), Using an equivalent source with positivity for low-latitude reduction to the pole without striation, *GEOPHYSICS*, *79*(6), J81–J90, doi:10.1190/geo2014-0134.1.

Lima, E. A., B. P. Weiss, L. Baratchart, D. P. Hardin, and E. B. Saff (2013), Fast inversion of magnetic field maps of unidirectional planar geological magnetization, *J. Geophys.*

Res.: Solid Earth, 118(6), 2723–2752, doi:10.1002/jgrb.50229.

Lima, E. A., A. C. Bruno, H. R. Carvalho, and B. P. Weiss (2014), Scanning magnetic tunnel junction microscope for high-resolution imaging of remanent magnetization fields, *Measurement Science and Technology, 25*(10), 105,401, doi:10.1088/0957-0233/25/10/105401.

Mareschal, J. C. (1985), Inversion of potential field data in fourier transform domain, *Geophysics, 50*(4), 685–691, doi:10.1190/1.1441943.

Mendonça, C. A. (1992), Interpolação de dados de campo potencial através da camada equivalente, Ph.D. thesis, Universidade Federal do Pará, Belém do Pará, Brazil.

Mendonça, C. A., and J. B. C. Silva (1994), The equivalent data concept applied to the interpolation of potential field data, *GEOPHYSICS, 59*(5), 722–732, doi:10.1190/1.1443630.

Mendonça, C. A., and J. B. C. Silva (1995), Interpolation of potentialfield data by equivalent layer and minimum curvature: A comparative analysis, *GEOPHYSICS, 60*(2), 399–407, doi:10.1190/1.1443776.

Nagata, T. (1961), *Rock magnetism*, second edition ed., Maruzen.

Nagy, D., G. Papp, and J. Benedek (2000), The gravitational potential and its derivatives for the prism, *Journal of Geodesy, 74*(7-8), 311–326, doi:10.1007/s001900000116.

Oda, H., and C. Xuan (2014), Deconvolution of continuous paleomagnetic data from pass-through magnetometer: A new algorithm to restore geomagnetic and environmental information based on realistic optimization, *Geochemistry, Geophysics, Geosystems, 15*(10), 3907–3924, doi:10.1002/2014GC005513.

Oda, H., A. Usui, I. Miyagi, M. Joshima, B. P. Weiss, C. Shantz, L. E. Fong, K. K. McBride, R. Harder, and F. J. Baudenbacher (2011), Ultrafine-scale magnetostratigraphy of marine ferromanganese crust, *Geology*, *39*(3), 227–230, doi:10.1130/G31610.1.

Oliveira Jr., V. C., V. C. F. Barbosa, and L. Uieda (2013), Polynomial equivalent layer, *GEOPHYSICS*, *78*(1), G1–G13, doi:10.1190/geo2012-0196.1.

Pérez, F., and B. E. Granger (2007), IPython: A System for Interactive Scientific Computing, *Computing in Science & Engineering*, *9*(3), 21–29, doi:10.1109/MCSE.2007.53.

Pozzi, J. P., and E. Thellier (1963), *Electrotechnique - Sur Des Perfectionnements Recents Apportes Aux Magnetometres A Tres Haute Sensibilite Utilises en Mineralogie Magnetique et en Paleomagnetisme*, vol. 257, second edition ed., C. R. Heb. Séances Acad. Sci.

Roth, B. J., N. G. Sepulveda, and J. P. Wikswo (1989), Using a magnetometer to image a two-dimensional current distribution, *J. Appl. Phys. (Melville, NY, U. S.)*, *65*(1), 361–372, doi:10.1063/1.342549.

Silva, J. B. C. (1986), Reduction to the pole as an inverse problem and its application to low-latitude anomalies, *GEOPHYSICS*, *51*(2), 369–382, doi:10.1190/1.1442096.

Tikhonov, A. N., and V. Y. Arsenin (1977), *Solutions of Ill-Posed Problems (Scripta series in mathematics)*, V. H. Winston & Sons.

Turner, G., J. Rasson, and C. Reeves (2015), 5.04 - observation and measurement techniques, in *Treatise on Geophysics (Second Edition)*, edited by G. Schubert, second edition ed., pp. 91 – 135, Elsevier, Oxford, doi:10.1016/B978-0-444-53802-4.00098-1.

Uehara, M., and N. Nakamura (2007), Scanning magnetic microscope system utilizing a magneto-impedance sensor for a nondestructive diagnostic tool of geological samples,

Rev. Sci. Instrum., *78*(4), doi:10.1063/1.2722402.

Uehara, M., and N. Nakamura (2008), Identification of stable remanence carriers through a magneto-impedance scanning magnetic microscope, *Stud. Geophys. Geod.*, *52*(2), 211–223, doi:10.1007/s11200-008-0014-2.

Uieda, L., V. C. Oliveira Jr., and V. C. F. Barbosa (2013), Modeling the earth with fatiando a terra, in *Proceedings of the 12th Python in Science Conference*, edited by S. van der Walt, J. Millman, and K. Huff, pp. 96 – 103.

Usui, Y., M. Uehara, and K. Okuno (2012), A rapid inversion and resolution analysis of magnetic microscope data by the subtractive optimally localized averages method, *Comput. Geosci.*, *38*(1), 145–155, doi:10.1016/j.cageo.2011.05.001.
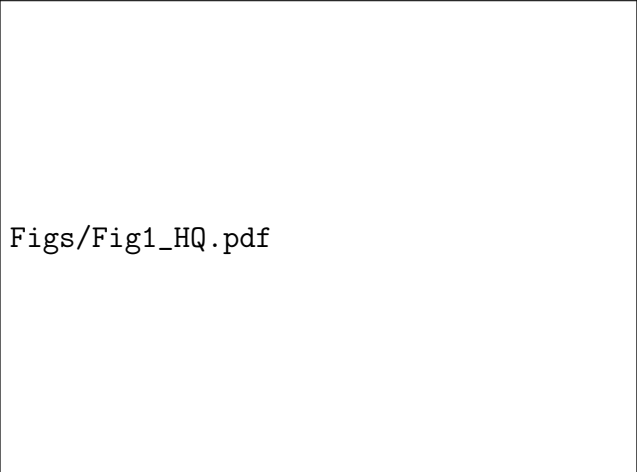
Van Der Voo, R. (1993), *Paleomagnetism of the Atlantic, Tethys and Iapetus oceans*.

Von Frese, R. R. B., W. J. Hinze, and L. W. Braile (1981), Spherical earth gravity and magnetic anomaly analysis by equivalent point source inversion, *Earth and Planetary Science Letters*, *53*(1), 69 – 83, doi:10.1016/0012-821X(81)90027-3.

Walt, S., S. C. Colbert, and G. Varoquaux (2011), The numpy array: A structure for efficient numerical computation, *Computing in Science & Engineering*, *13*(2), 22–30, doi:10.1109/MCSE.2011.37.
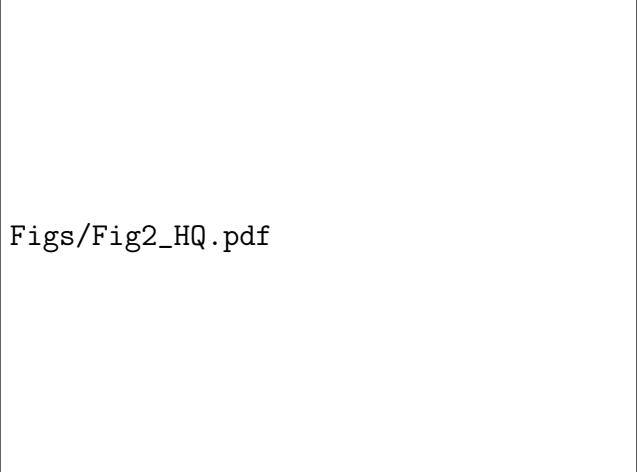
Weiss, B. P., E. A. Lima, L. E. Fong, and F. J. Baudenbacher (2007a), Paleointensity of the earth's magnetic field using {SQUID} microscopy, *Earth Planet. Sci. Lett.*, *264*(12), 61–71, doi:10.1016/j.epsl.2007.08.038.

Weiss, B. P., E. A. Lima, L. E. Fong, and F. J. Baudenbacher (2007b), Paleomagnetic analysis using squid microscopy, *J. Geophys. Res.: Solid Earth*, *112*(B9), doi:10.1029/2007JB004940.

Figs/Fig1_HQ.pdf

Figure 1. Main coordinate system (MCS). The origin of this coordinate system coincides with the center of the sample (gray prisms and rectangles). The gray juxtaposed prisms represent regions with constant and uniform magnetization. The sample is shown from (a) a superior perspective view and also from two side views represented in (b) and (c).

Figs/Fig2_HQ.pdf

Figure 2. Schematic representation of the rectangular rock sample shown in Figure 1. The gray juxtaposed prisms represent regions with constant and uniform magnetization. The magnetic induction produced by the rock sample is measured on the planes located (a) above, (b) on the right side, (c) below and (d) on the left side of the sample. These observation planes are identified, respectively, by the index $\alpha = 0, 1, 2, 3$.
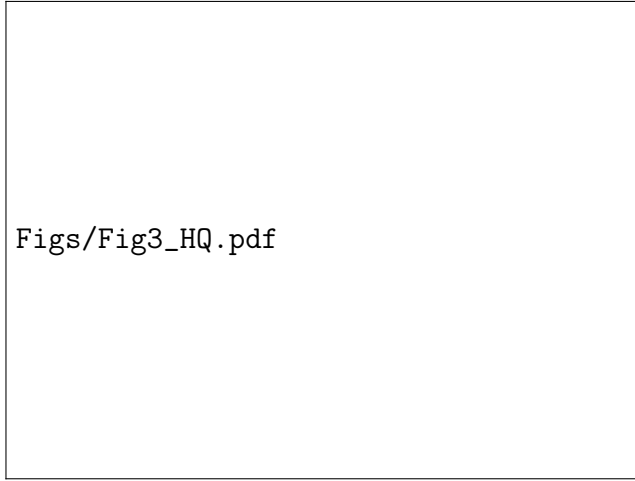
Figs/Fig3_HQ.pdf

Figure 3. 2D sketch of the coordinate systems. (a) MCS (Figure 1). (b), (c), (d) and (e) Local coordinate systems (LCS's) of the measured magnetic induction on the four observation planes, $\alpha = 0, 1, 2, 3$ (dashed lines), which are located at the same distance h from the surface of the sample. Note that there is a different LCS for the measured magnetic induction on each observation plane (dashed lines). The quantities referred to the LCS's are marked with a prime ($'$). The x-axis of the MCS (Figure 1) coincides with the x'-axes of all LCS's. The x- and x'-axes point into the plane of paper.

Figure 4.   Schematic representation of misalignments during the acquisition of magnetic data. The projections of the edges and the center of the sample onto the observation plane are represented, respectively, by the open rectangles and black dots. The grey rectangles represent the area containing the magnetic data on the observation plane. x' and y' represent the axes and the open dot shown in (b) represents the origin of the LCS (Figure 3). (a) Example of acquisition without misalignment. In this case, the center of the sample coincides with the origin of the LCS and the edges of the sample are aligned with the axes of the LCS. (b) Example of acquisition presenting misalignments. In this case, the relative position of the center of the sample with respect to the origin of the LCS is displaced by $\Delta x'$ and $\Delta y'$ along, respectively, the x' and y' axes. Besides, the edges of the sample are rotated anticlockwise with respect to the axes of the LCS. (c) Corrected position of the sample with respect to the magnetic data obtained on the observation plane.
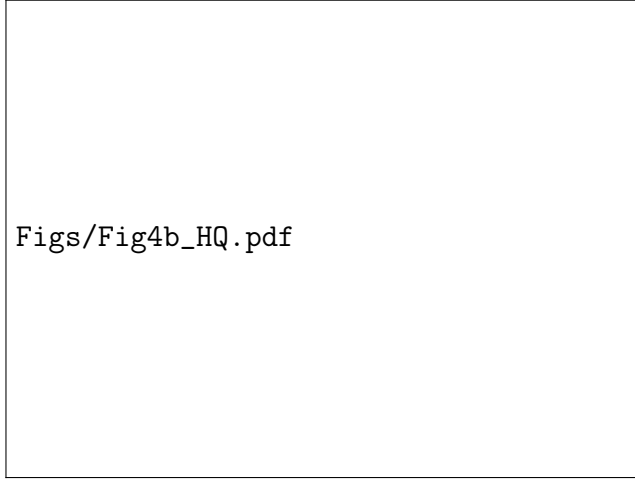
Figs/Fig4b_HQ.pdf

Figure 5. Schematic representation of the discretization used for approximating the integral 5 by the summation 6. (a) Magnetic sensor with active area A (light grey square) located at a distance h of the sample (grey prisms), on a particular observation plane α (Figures 2 and 3). (b) Detailed representation of the sensor active area A centered at the observation point (x_i, y_i) (black circle). The square active area of the sensor is discretized into a regular grid of Q square cells (limited by the dashed lines). Each cell is centered at a point (x_j, y_j), $j = 1, ..., Q$, (open circles) and has an area $\Delta A = A/Q$. The points (x_i, y_i) and (x_j, y_j) can be either referred to a specific LCS or to the MCS (Figure 3).

Figs/Fig5_LQ.png

Figure 6.   Validation test. (a), (d), (g) and (j) Noise-corrupted magnetic data produced by the synthetic sample (not shown) on the observation planes $\alpha = 0, 1, 2$ and 3, respectively. (b), (e), (h), (k) Predicted data produced by the estimated magnetization distribution on the observation planes $\alpha = 0, 1, 2$ and 3, respectively. The estimated magnetization distribution was obtained by inverting the magnetic data located on the four observation planes. (c), (f), (i) and (l) Normalized histograms of the residuals between the predicted data shown in (b), (e), (h), (k) and the noise-corrupted magnetic data shown in (a), (d), (g), (j). The normalization consists in subtracting from the residuals its sample mean μ and dividing the result by its sample standard deviation σ. The values are in μT.

Figure 7. Validation test. Comparison between the true (red dots) and estimated (blue and black dots) magnetization (a) intensity, (b) inclination and (c) declination. The estimated magnetization distribution obtained by inverting the magnetic data on the four planes $\alpha = 0, 1, 2, 3$ is represented by the black dots and black dashed lines. The three sets of blue dots and dashed lines represent the estimated magnetization distribution obtained by inverting the magnetic data located on a single plane ($\alpha = 0$), two planes ($\alpha = 0, 1$) and three planes ($\alpha = 0, 1, 2$) are plotted, respectively, with high, intermediate and low transparency. The values are plotted along the x-axis, at the center of each prism forming the interpretation model. The black dashed lines in (b) and (c) indicate the $0°$ value.

Figs/Fig7_LQ.png

Figure 8.   Pre-processing errors test. (a), (d), (g) and (j) Noise-corrupted magnetic data produced by the synthetic sample (not shown) on the observation planes $\alpha = 0, 1, 2$ and 3, respectively. (b), (e), (h), (k) Predicted data produced by the estimated magnetization distribution obtained by inversion on the observation planes $\alpha = 0, 1, 2$ and 3, respectively. The estimated magnetization distribution was obtained by inverting the magnetic data located on the four observation planes. (c), (f), (i) and (l) Normalized histograms of the residuals between the predicted data shown in (b), (e), (h), (k) and the noise-corrupted magnetic data shown in (a), (d), (g), (j). The normalization consists in subtracting from the residuals its sample mean μ and dividing the result by its sample standard deviation σ. The values are in μT.

Figure 9. Pre-processing errors test. Comparison between the true (red dots) and estimated (blue and black dots) magnetization (a) intensity, (b) inclination and (c) declination. The estimated magnetization distribution obtained by inverting the magnetic data on the four planes $\alpha = 0, 1, 2, 3$ is represented by the black dots and black dashed lines. The three sets of blue dots and dashed lines represent the estimated magnetization distribution obtained by inverting the magnetic data located on a single plane ($\alpha = 0$), two planes ($\alpha = 0, 1$) and three planes ($\alpha = 0, 1, 2$) are plotted, respectively, with high, intermediate and low transparency. The values are plotted along the x-axis, at the center of each prism forming the interpretation model. The black dashed lines in (b) and (c) indicate the $0°$ value.

Figs/Fig9_LQ.png

Figure 10. Sensor-to-sample distance test. (a), (d), (g) and (j) Noise-corrupted magnetic data produced by the synthetic sample (not shown) on the observation planes $\alpha = 0, 1, 2$ and 3, respectively. (b), (e), (h), (k) Predicted data produced by the estimated magnetization distribution obtained by inversion on the observation planes $\alpha = 0, 1, 2$ and 3, respectively. The estimated magnetization distribution was obtained by inverting the magnetic data located on the four observation planes. (c), (f), (i) and (l) Normalized histograms of the residuals between the predicted data shown in (b), (e), (h), (k) and the noise-corrupted magnetic data shown in (a), (d), (g), (j). The normalization consists in subtracting from the residuals its sample mean μ and dividing the result by its sample standard deviation σ. The values are in μT.

Figure 11.   Sensor-to-sample distance test. Comparison between the true (red dots) and estimated (blue and black dots) magnetization (a) intensity, (b) inclination and (c) declination. The estimated magnetization distribution obtained by inverting the magnetic data on the four planes $\alpha = 0, 1, 2, 3$ is represented by the black dots and black dashed lines. The three sets of blue dots and dashed lines represent the estimated magnetization distribution obtained by inverting the magnetic data located on a single plane ($\alpha = 0$), two planes ($\alpha = 0, 1$) and three planes ($\alpha = 0, 1, 2$) are plotted, respectively, with high, intermediate and low transparency. The values are plotted along the x-axis, at the center of each prism, assuming the interpretation model. The black dashed lines in (b) and (c) indicate the 0° value.
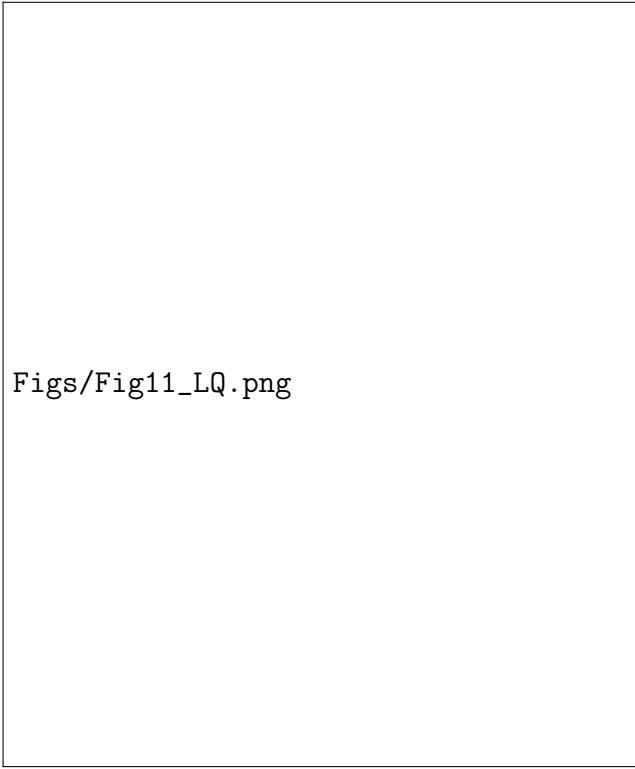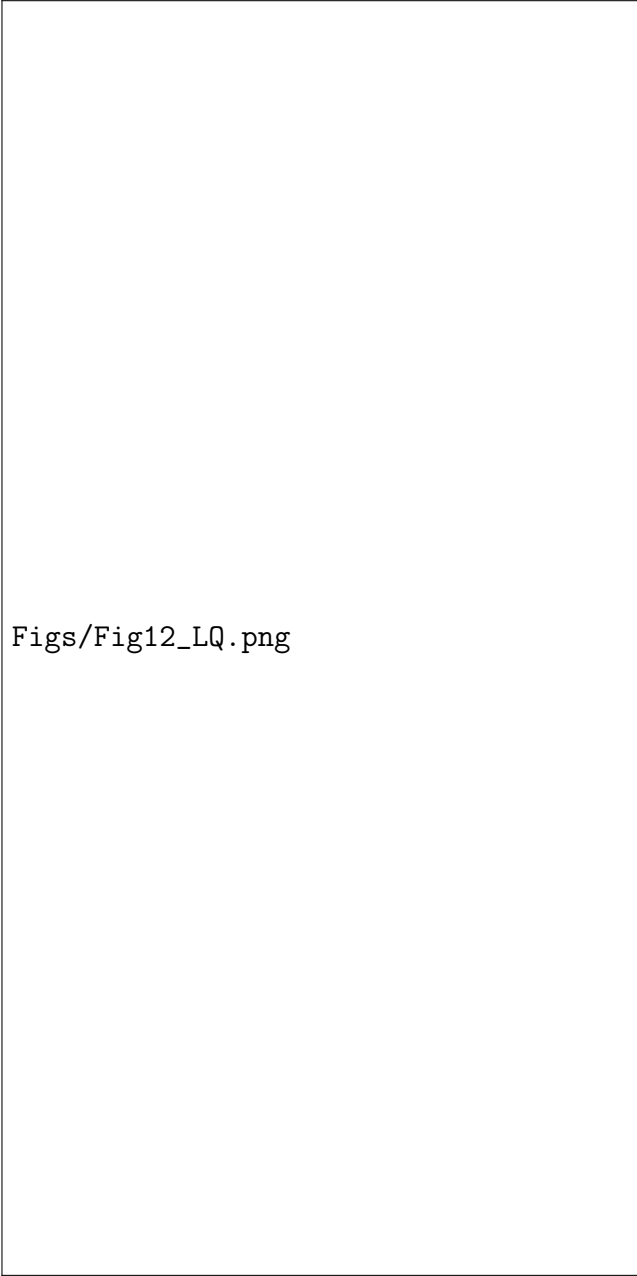
Figure 12.   Marine ferro-manganese crust sample. (a), (d), (g) and (j) Noise-corrupted magnetic data produced by the synthetic sample (not shown) on the observation planes $\alpha = 0, 1, 2$ and 3, respectively. (b), (e), (h), (k) Predicted data produced by the estimated magnetization distribution obtained by inversion on the observation planes $\alpha = 0, 1, 2$ and 3, respectively. The estimated magnetization distribution was obtained by inverting the magnetic data located on the four observation planes. The color scales are slightly saturated for improving the visualization. (c), (f), (i) and (l) Normalized histograms of the residuals between the predicted data shown in (b), (e), (h), (k) and the noise-corrupted magnetic data shown in (a), (d), (g), (j). The normalization consists in subtracting from the residuals its sample mean μ and dividing the result by its sample standard deviation σ. The values are in nT.

Figure 13. Marine ferro-manganese crust sample. Comparison between the true (red dots) and estimated (blue and black dots) magnetization (a) intensity, (b) inclination and (c) declination. The estimated magnetization distribution obtained by inverting the magnetic data on the four planes $\alpha = 0, 1, 2, 3$ is represented by the black dots and black dashed lines. The three sets of blue dots and dashed lines represent the estimated magnetization distribution obtained by inverting the magnetic data located on one the plane $\alpha = 0$, planes $\alpha = 0, 1$ and planes $\alpha = 0, 1, 2$ are plotted, respectively, with high, intermediate and low transparency. The values are plotted along the x-axis at the center of each prism forming the interpretation model. The black dashed lines in (b) and (c) indicate the $0°$ value.

Figs/Fig13_HQ.pdf

Figure 14. Manufactured sample. (a) Four prisms forming the sample. The IRM magnetization of these prisms are approximately parallel to the vertical planes represented in grey. (b) Magnetization (thick arrows) of the prisms on the vertical planes shown in (a). (c) Resultant sample obtained by juxtaposing the magnetized prisms. The numbers indicate the index of each prism, whose magnetization is represented by the thick arrows. The inclination and declination values of the IRM within each prism is shown in Table 3. The resulting sample is referred to a MCS (Figure 1) with origin represented by the black dot and axes x and z represented by the thin arrows.
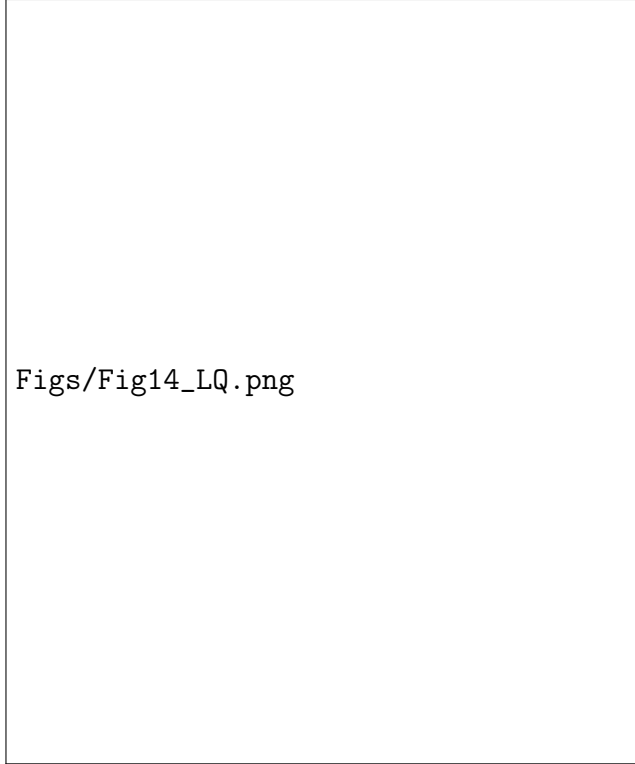
Figure 15. Application to real data. (a), (d), (g) and (j) Observed magnetic data produced by the synthetic sample (not shown) on the observation planes $\alpha = 0, 1, 2$ and 3, respectively. (b), (e), (h), (k) Predicted data produced by the estimated magnetization distribution obtained by inversion on the observation planes $\alpha = 0, 1, 2$ and 3, respectively. The estimated magnetization distribution was obtained by inverting the magnetic data located on the four observation planes. (c), (f), (i) and (l) Normalized histograms of the residuals between the predicted data shown in (b), (e), (h), (k) and the observed magnetic data shown in (a), (d), (g), (j). The normalization consists in subtracting from the residuals its sample mean μ and dividing the result by its sample standard deviation σ. The values are in μT.

Figure 16.   Application to real data. Estimated magnetization (a) intensity, (b) inclination

and (c) declination. The estimated magnetization distribution obtained by inverting the mag-

netic data on the four planes $\alpha = 0, 1, 2, 3$ is represented by the black dots and black continuous

lines. The three sets of blue dots and dashed lines represent the estimated magnetization dis-

tribution obtained by inverting the magnetic data located on a single plane ($\alpha = 0$), two planes

($\alpha = 0, 1$) and three planes ($\alpha = 0, 1, 2$) are plotted, respectively, with high, intermediate and

low transparency. The values are plotted along the x-axis, at the center of each prism forming

the interpretation model. The continuous (vertical) black lines divide the estimated values rep-

resenting each prism forming the sample. The numbers indicate the index of each prism (Figure

14c and Table 3. The black dashed (horizontal) lines in (b) indicate the values $-90°$, $0°$, $45°$

and $90°$. The black dashed (horizontal) lines in (c) indicate the values $0°$ and $180°$. The esti-

Table 1. Transformations between the LCS's and the MCS[a]

	Cartesian coordinate		Field component	
α	y	z	y	z
0	y'	z'	–	z'
1	$-z'$	y'	$-z'$	–
2	$-y'$	$-z'$	–	$-z'$
3	z'	$-y'$	z'	–

[a] Correspondence between the Cartesian coordinates y' and z' and the Cartesian coordinates y and z as well as between the z'-component and the y- or z-component of the magnetic induction. The quantities marked with prime ($'$) are referred to the LCS's (Fig. 3b-e) while the quantities without prime ($'$) are referred to the MCS (Fig. 3a).

Table 2. Misalignment parameters[a]

α	θ (°)	$\Delta x'$ (μm)	$\Delta y'$ (μm)
0	5.5	0	-100
1	3.0	500	-400
2	3.0	200	1000
3	4.0	200	500

[a] Parameters θ, $\Delta x'$ and $\Delta y'$ (Figure 4b) defining the misalignments in the magnetic data produced by the synthetic sample described in section 3.

Table 3. Approximated IRM orientation within the prisms forming synthetic sample[a]

index	I (°)	D (°)
0	45	180
1	45	0
2	-90	–
3	90	–

[a] IRM inclination (I) and declination (D) of the prisms forming the synthetic sample that was manufactured in laboratory. Each prism is indicated by an index, according to the Figure 14c.